Three-dimensional deformation dynamics of porous titanium under uniaxial compression

H.W. Chai [a], Z.L. Xie [b,*], Z.D. Feng [a], S.N. Luo [b], J.Y. Huang [a,*]

[a] *The Peac Institute of Multiscale Sciences, Chengdu, Sichuan, PR China*
[b] *School of Materials Science and Engineering, Southwest Jiaotong University, Chengdu, Sichuan, PR China*

ARTICLE INFO

ABSTRACT

In situ, synchrotron-based micro computerized tomography is used to investigate three-dimensional (3D) deformation dynamics of open-cell porous titanium under uniaxial compression. The 3D pore structures are captured, segmented, and transformed into separated pores (spheres) connected by throats (bars) according to the pore network model (PNM). Pore and throat size distributions are quantified via the PNM, while pore shape and orientation distributions, via gyration tensor analysis. After yield, the mean values of equivalent diameter, sphericity and aspect ratios of the pores decrease as deformation progresses, indicating increased pore anisotropy. However, the number and equivalent diameter of the throats decrease even at the elastic stage, and the average diameter decreases approximately linearly with increasing bulk strain. The collapse of individual pores is tracked, and the pores with their longest axes aligned perpendicular to the loading direction are prone to compaction compared to those aligned parallel to the loading direction, because of different stress concentrations. Microstructure-based finite element (FE) analysis reproduces the overall deformation characteristics observed in the experiments. The deformation mechanisms and FE model may be useful for guiding material assessment and design related to porous Ti.

1. Introduction

Porous Ti and Ti-alloys have been increasingly used in biomedical and aeronautical applications, due to their excellent mechanical properties, biocompatibility and corrosion resistance [1–3]. Compared to the full-density counterpart, the bone-like porous structure in porous Ti can diminish the "stress-shielding" effect [1,4] thanks to its better mechanical compatibility, and enhance long-term biofixation via tissue ingrowth. Nevertheless, pores induce stress/strain localizations under external stimuli [5–7], and undermine damage tolerance. Deformation and collapse of pores dominate the mechanical performance of porous materials [8]. However, three-dimensional (3D), pore-scale deformation dynamics of porous Ti has been rarely studied yet.

The bulk mechanical properties of porous Ti has been extensively investigated [9–12]. The elastic modulus and yield strength of porous Ti decrease with increasing porosity, following the Gibson-Ashby model [8]. The porosity effect has been relatively well understood. Apart from porosity, pore morphology, including shape, size and orientation, may also affect the mechanical properties of porous Ti [9,12]. For instance, porous Ti with spherical pores exhibits a higher resistance to pore

collapse, and thus a higher compressive strength than that with needle-shaped or ellipsoidal pores [9]. Pore orientation determines the local loading geometry of the Ti skeleton enclosing pores [13]. The porous Ti with unidirectional cylindrical pores displays pronounced anisotropy [14]. The compressive strength appears higher for porous Ti loaded along the long axial direction of pores than along the radial direction of pores. The pore size effect is complex and contradictory for porous Ti materials fabricated via different routes [10,15]. Overall, previous studies focused on the bulk mechanical properties of porous Ti. The mechanisms for three-dimensional (3D) pore deformation and collapse in porous Ti with random pores under compression were rarely touched, largely due to the lack of *in situ*, microscopic measurements on deformation dynamics of porous Ti. The influence of pore morphology on local pore collapse and bulk plasticity is of particular interest.

Micro- or mesoscopic observations on deformation of porous Ti commonly resort to two-dimensional (2D) postmortem analysis via scanning electron microscopy [10,16]. However, microstructures of pores are 3D in nature; there are distinct differences between 2D and 3D quantification of local density and pore morphology of porous materials [17]. Micro computerized tomography (CT) has been widely used to
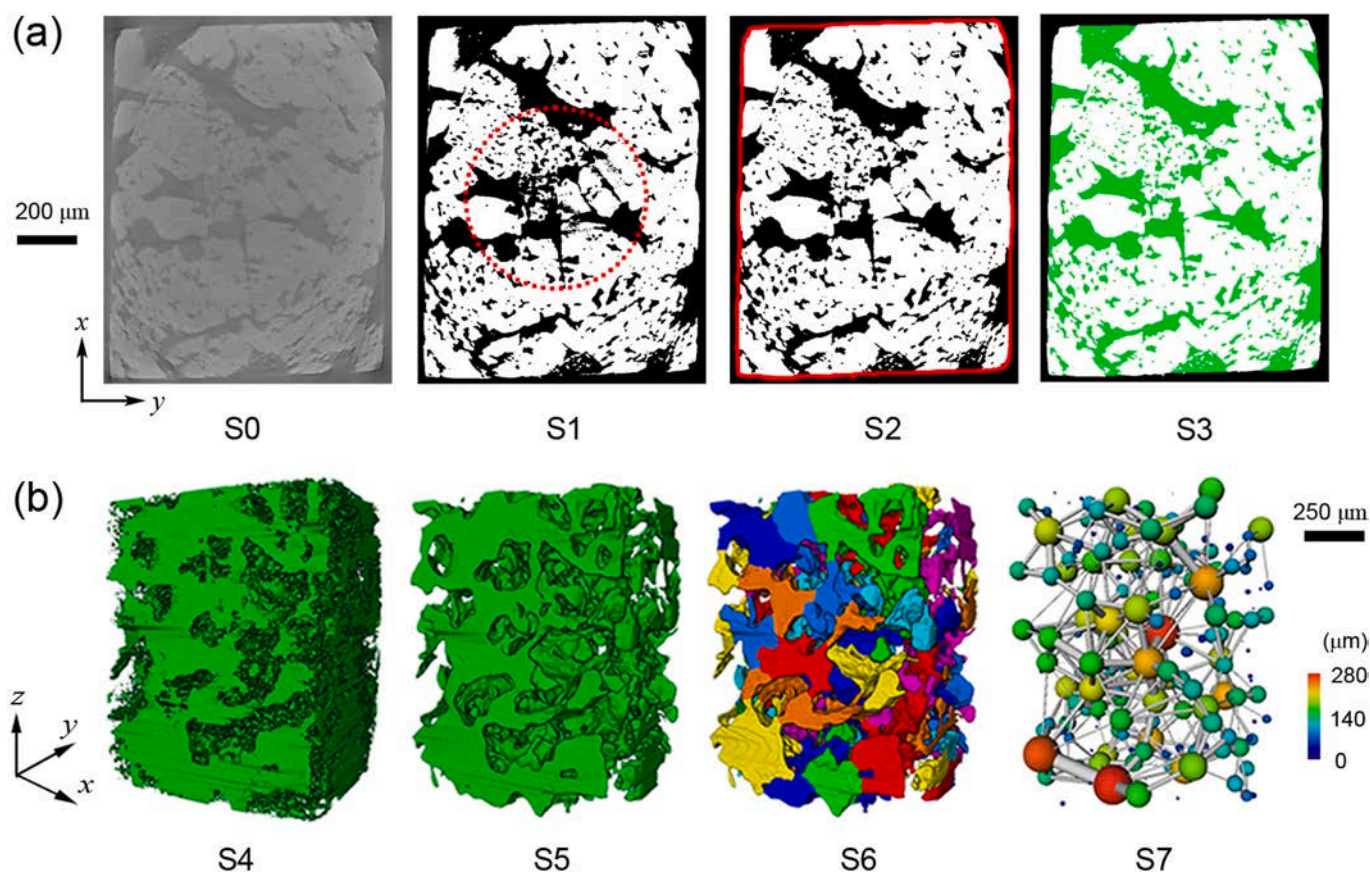

Fig. 1. (a) Image processing procedure to render the Ti skeleton and pore structures. S0: gray-scale *xy* slice; S1: global threshold segmentation; S2: iterative local threshold segmentation applied to the central areas; S3: identifying solid phase (white) and pore phase (green). (b) Segmentation and quantification of the pore structure. S4: 3D pore structure; S5: smoothed pore structure after removing tiny pores and sharp edges; S6: watershed segmentation; S7: equivalent pores (spheres) and throats (bars) according to the PNM. (For interpretation of the references to color in this figure legend, the reader is referred to the web version of this article.)

characterize 3D cellular structures [18–22]. Porous Ti has pores of tens to hundreds of microns and the absorption coefficient of Ti is high for X-rays. Therefore, mapping 3D structures of porous Ti requires high spatial resolution (~1 μm) and high energy X-rays for CT.

Synchrotron-based, *in situ* micro CT has been developed to characterize microstructures of porous materials [23,13,24]. Synchrotron CT can provide deformation details of cellular structures at a micron scale, and is advantageous for tracking 3D pore deformation. Evolution of the morphology of pore networks is useful for understanding deformation mechanisms of porous Ti. However, in addition to the lack of high-quality 3D data, how to quantify the pore morphology of deformed open-cell porous Ti is another nontrivial problem [25–28]. Numerical models based on 3D porous structures have been adopted to capture the actual meso-scale geometry [29,30]. Finite element (FE) modelling with real 3D structures of porous Ti was rarely reported partly owing to high computational cost [31]; 2D slices [18] or quasi-real 3D porous structures [32,33] were frequently used instead.

In the present study, uniaxial compression tests are conducted on a powder-sintered porous Ti, with a home-made material test system (MTS). *In situ*, synchrotron-based, micro CT is used to map the evolution of 3D microstructures. The pore network model (PNM) [34] and gyration tensor analysis [13] are adopted to quantify the morphology of pore structures throughout the deformation process. It is noteworthy that the number and size of interconnections between pores start to decrease even at the elastic deformation stage. The deformation mechanisms and FE model can help guide material assessment and design related to porous Ti.

2. Materials and methods

2.1. Materials

Commercially available, open-cell porous Ti is studied in this work. It is fabricated via powder metallurgy with angular Ti powders. Test samples are harvested from the as-received "foam" blocks via electrical discharge machining. X-ray diffraction (XRD; PANalytical Empyrean; Cu K_α) analysis shows that the matrix is mainly of the α-Ti phase. The Young's modulus and bulk density at ambient conditions are measured as 13±2 GPa and 3.16±0.22 g/cm^3, respectively.

2.2. In situ CT

A home-made MTS is implemented with micro CT at the beamline 2-BM, Advanced Photon Source, USA. The experimental setups and procedures are detailed in Refs. [13] and [35]. The nominal spatial resolution is 1.625 μm per pixel, sufficient for characterizing deformation details of pores [36]. The sample dimensions are 1.5 mm along the loading direction or the *z*-axis, 1.2 mm along the *x*-axis and 0.9 mm along the *y*-axis. The sample is sandwiched between two steel platens. Upon loading, once the preset displacement level is reached, the loading is paused and a CT scan is conducted on the deformed sample after the platen force reaches a steady state (within about 30 s). The X-ray energy is set at 35 keV, the sample-to-scintillator distance is 60 mm, and the exposure time is 350 ms. Each tomography scan captures 1500 projections within the 0°–180° range, which are then reconstructed into a 3D image with an open-source software *TomoPy* [37]. The force-–displacement curve recorded by MTS is used to derive the axial

Table 1
Material parameters of the full-density Ti for FE modelling.

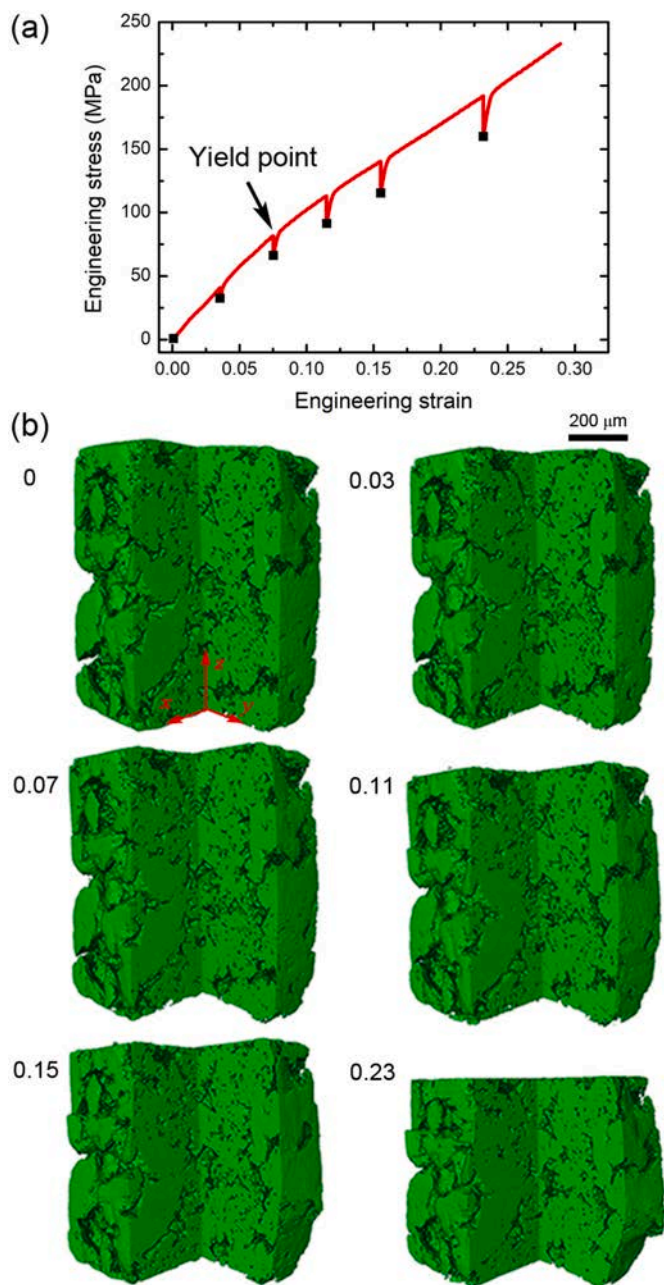|	
Bulk density (kg m^{-3})	4510
Young's modulus (GPa)	106
Poisson's ratio	0.34
A (MPa)	261.8
B (MPa)	995.1
n	0.826

Fig. 2. In situ CT characterization of the porous Ti sample. (a) Stress–strain curve. The stress drops correspond to the pauses for CT scans. (b) 3D reconstructions of porous Ti at different strains as indicated, corresponding to diamonds in (a).

stress–strain curve. The loading speed is set at 1.5 μm s^{-1}, resulting in a nominal strain rate of 0.001 s^{-1}.

To extract 3D pore structures, a reconstructed image (S0) is

processed in three steps (Fig. 1a). S0 is first binarised into the solid phase (black in S1) and air (white in S1) via global threshold segmentation (TS). Then, the central area of S1 (marked by the dashed circle) is improperly segmented (a part of the solid phase is mistaken as air) via global TS, since there exists a positive gradient in grayscale value from center to edge. Iiterative local TS is applied to the central area in S1 to properly segment the whole image (S2). Finally, a convex hull [38] enclosing the solid phase is constructed (the red line in S2), and the air within the convex hull is identified as the pores (green in S3).

The 3D pore structure (S4) is processed further to quantify pore morphology in three steps. First, the pore surfaces are properly smoothed (S5) to remove the sharp edges and corners and micro fissures are filled. This results in a minor (<3%) loss in porosity but simplifies the pore structure considerably. Then, classic watershed segmentation is
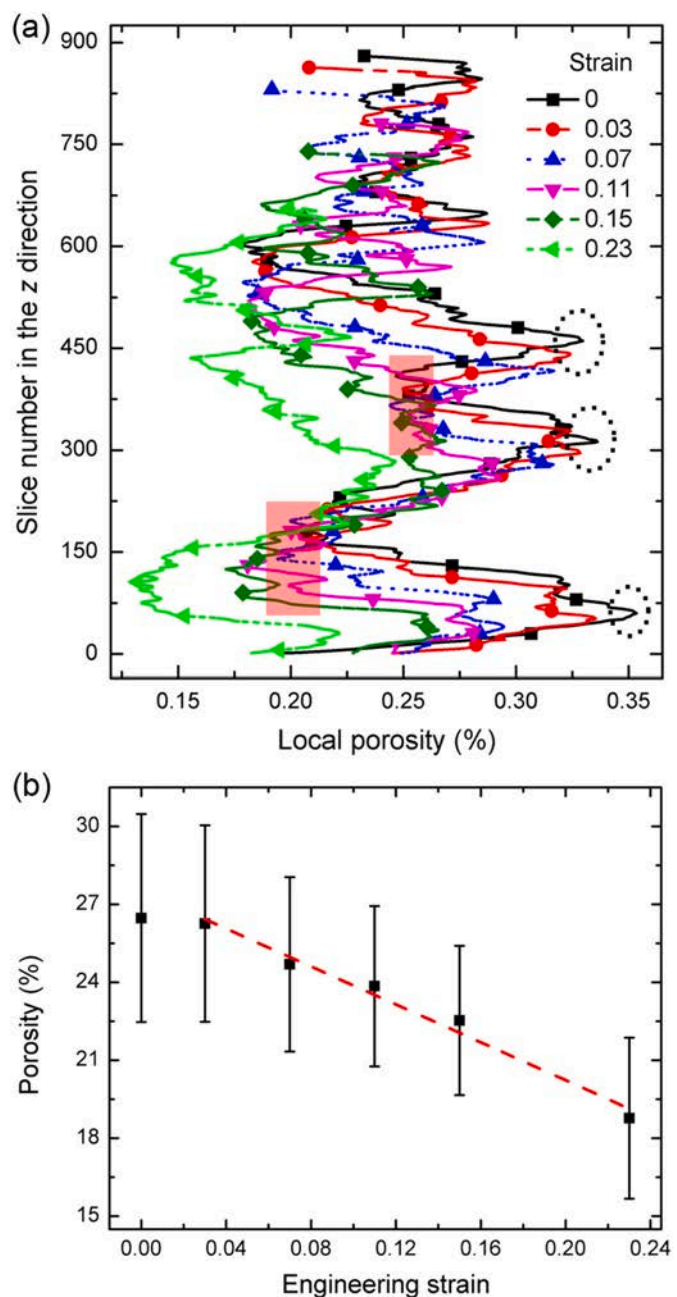

Fig. 3. (a) Local porosity distributions along the loading axis at different bulk strains. (b) Overall porosity as a function of bulk strain. The dashed line is a linear fit to the experimental data.

applied to segment the interconnected pore network into artificially separated individual pores (S6). Lastly, the segmented pores are transformed into equivalent spheres (pores) connected with bars (throats) (S7) according to the PNM [34,39].

2.3. Finite element modelling

FE modelling of deformation of the 3D porous structure is used to help analyze stress distribution across the Ti matrix. The initial 3D structure of the porous sample is used as the starting configuration for FE analysis. The binarized volume data is firstly converted into a surface mesh with triangular elements. In order to reduce the computational cost, a mesh size of around 10 μm is used. The surface mesh is refined with interaction, aspect ratio, and holes considered, and the sharp edges and corners of macro pores are smoothed. The surface mesh is finally converted into a volume mesh. The meshed volume has a total of 665,051 elements. The linear tetrahedron element is used for calculation. The volume mesh configuration is then imported for FE analysis along with material properties of the full-density Ti, and boundary and loading conditions.

The Johnson-Cook model is used to describe the relationship between flow stress σ_p and equivalent plastic strain ε_p as

$$\sigma_p = A + B\varepsilon_p^n, \tag{1}$$

where A, B and n are material parameters. The material parameters for full-density pure Ti [40] are listed in Table 1. The sample is sandwiched between two rigid plates, and the top plate is allowed to move downward/upward along the z-axis or compressing direction. A friction coefficient of 0.2 is set for the contact between the plate and sample.

3. Results and discussions

3.1. In situ CT measurements

The axial engineering stress−strain curve of the porous Ti sample along with the volume renderings at different strains are presented in Fig. 2. The stress–strain curve (Fig. 2a) exhibits linear-elastic and plastic-hardening deformation stages similar to that of full-density Ti, but with a significantly reduced elastic modulus and yield strength (72 MPa). The 3D image of the initial sample shows that macropores ($\sim$120 μm) coexist with a large number of micropores ($\sim$10 μm), which has also been observed in aluminum foams [19,41]. These macropores are compacted gradually across the sample with increasing loading, while the micropores remain approximately unchanged away from the loading platen. The sample exhibits obvious lateral expansion during the plastic deformation stage.

To examine the deformation heterogeneity of the porous Ti sample, the local porosity distributions along the loading direction at different strains are calculated (Fig. 3a) [42]. The initial porosity distribution is inhomogeneous along the loading axis and exhibits multiple peaks (local maxima) and valleys (local minima). Upon loading, the porosity distribution changes little before the bulk strain (ε) reaches 0.03; after that, the local porosity decreases nonuniformly across the sample as deformation progresses. The peak regions (marked by the dashed ellipses) exhibit a higher porosity reduction with increasing strain, indicating larger deformation there. In contrast, the porosity of the valley regions (marked by the shaded rectangles) changes little. For example, the initial bimodal porosity distribution in the 300–600 slice layers becomes flat-topped at $\varepsilon = 0.15$, rendering a deformation band there. Fig. 3b presents the means (points) and standard deviations (error bars) of the porosity distributions at different bulk strains. For $\varepsilon > 0.03$, the overall porosity decreases linearly with increasing strain, consistent with previous studies [23]. The standard deviations also decrease with increasing strain, indicating decreased structural heterogeneity across the sample.
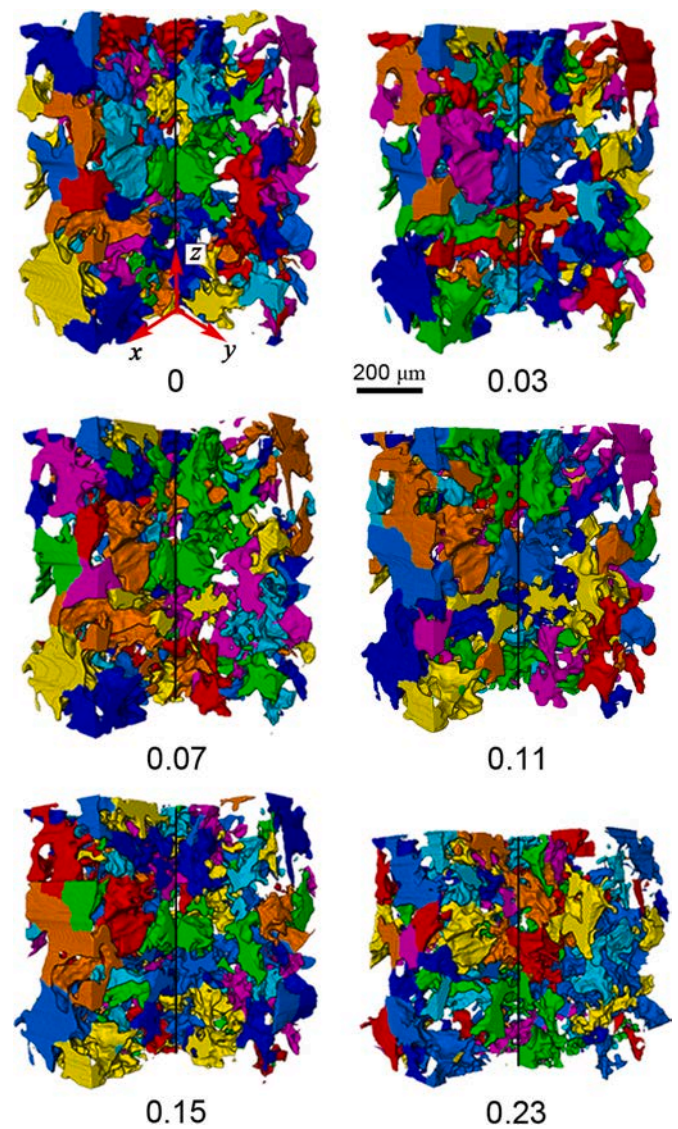

Fig. 4. Segmented pore structures at different bulk strains. Color-coding refers to different pores.

3.2. Pore morphology

Pore partitioning (Section 2.2) is applied to the binarised volume data at different bulk strains to separate connected pores. The segmented pore structures at different strains are illustrated in Fig. 4. The segmentation parameters are the same for all the configurations. The segmented pore structures are further analyzed with the PNM and gyration tensor analysis.

The equivalent pore (sphere) and throat (bar) networks derived from the PNM at different strains are shown in Fig. 5a. In the initial sample, the pores are interconnected by throats while the number of isolated pores (mainly small pores) is negligible. The pore-throat network changes little in the elastic deformation stage. After yield, pores and throats are gradually compacted, leading to considerable changes in the pore and throat morphologies. The number of isolated pores increases while the interconnectivity decreases (from 99% to 95%) with increasing strain. As shown in Fig. 5b, the mean equivalent diameters of pores (spheres) and throats (bars) decrease with increasing strain. The mean pore diameter decreases from 122 μm initially to 95 μm at $\varepsilon = 0.23$. The mean throat diameter decreases approximately linearly throughout the deformation process.

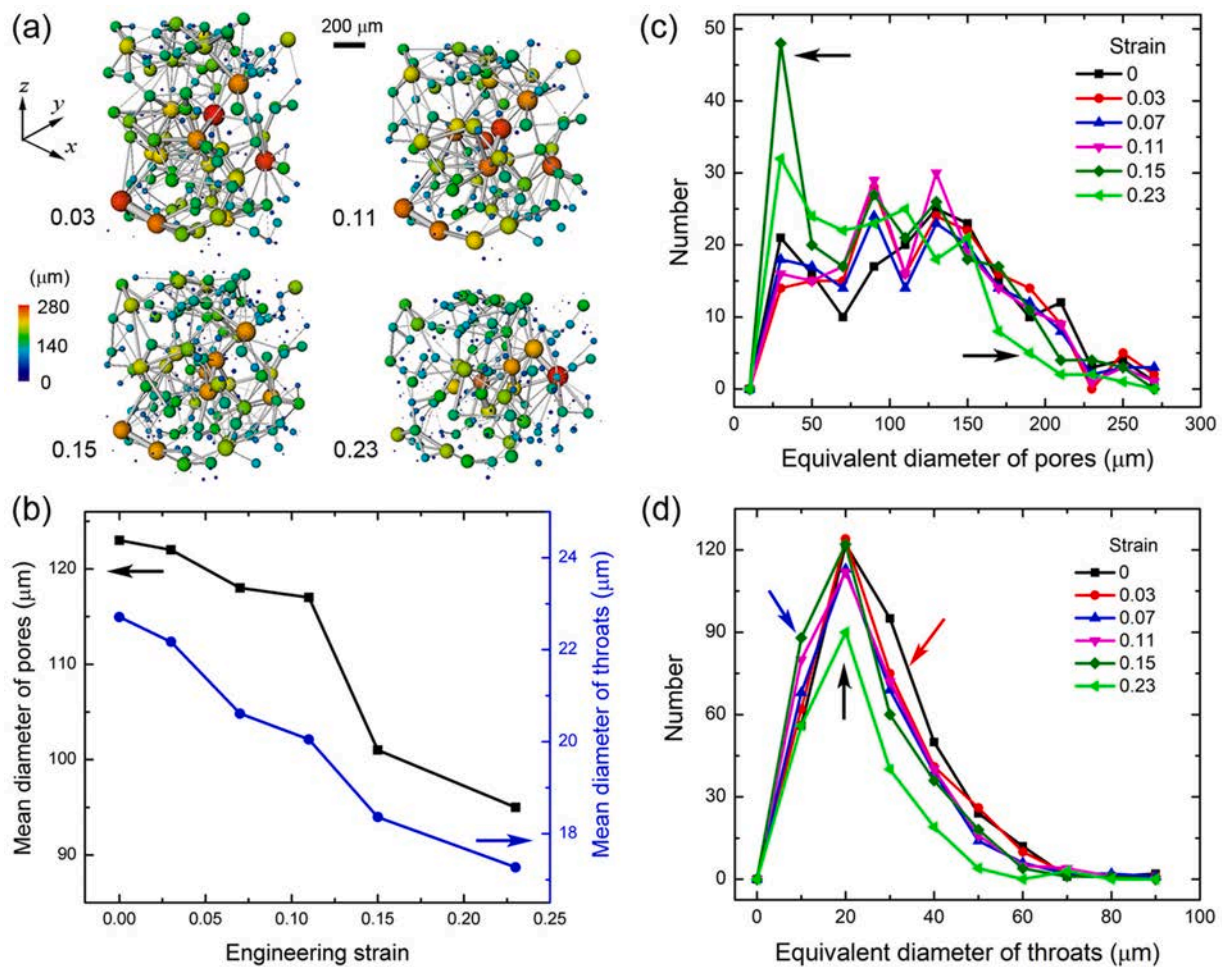The pore size distributions (Fig. 5c) remain unchanged except in the

Fig. 5. (a) Equivalent pore (sphere) and throat (bar) networks derived from the PNM at different strains. (b) Mean equivalent diameters of pores and throats as a function of strain. (c) and (d) Size distributions of pores (c) and throats (d) at different strains.

small size range, before the strain reaches 0.11. With increasing loading ($\varepsilon = 0$–0.11), the number of small pores (diameter $< 50\ \mu m$) decreases slightly, while that of pores with diameters 70–120 μm increases. The pore structure changes little during this deformation stage. At $\varepsilon = 0.15$, the number of small pores becomes two times higher than that at $\varepsilon = 0.11$ (marked by the left arrow in Fig. 5c) while that of large pores (diameter around 200 μm) decreases by about 70%, leading to a sharp drop in the mean pore diameter (Fig. 5b). The probable reason is that initially separated pore walls approach each other and come into contact during pore collapse, cutting a large pore into two or more smaller ones [19,42,13]. However, the number of pores with diameters smaller than 50 μm and larger than 170 μm (marked by the right arrow in Fig. 5c) decreases considerably at $\varepsilon = 0.23$, as a result of an overall compaction of pores across the sample. The total number of pores is reduced by ~15%, compared to that at $\varepsilon = 0.15$. The throat size distributions (Fig. 5d) at different strains show that the number of throats with diameters 20–40 μm decrease considerably in the strain range of 0–0.07 (marked by the red arrow in Fig. 5d), leading to a decrease in the mean throat diameter from 23 to 21 μm. Therefore, micro damage occurs in the porous Ti sample in the apparent elastic deformation stage (Fig. 2a). This reduction in throat size reduces the permeability and thus bioperformance of porous Ti scaffolds [43,4], even if the pore network remains mechanically stable. After yield, the number of throats increases slightly in the small-size range (marked by the blue arrow in Fig. 5d) in the 0.07–0.15 strain range, and then decreases significantly for all throat sizes at $\varepsilon = 0.23$ (marked by the black arrow in Fig. 5d). This is consistent with the evolution of pore size distributions except that

throats are compacted prior to pores.

Gyration tensor analysis [44,45] is adopted to characterize the shape (sphericity and aspect ratio) of pores. A characteristic ellipsoid is firstly constructed from the voxels of a pore. Three characteristic axes, $2a$, $2b$, and $2c$ ($a > b > c$), are then obtained. The sphericity S_G of a pore is defined as

$$S_G = 1 - \frac{1}{2}\frac{(a^2 - b^2)^2 + (a^2 - c^2)^2 + (b^2 - c^2)^2}{(a^2 + b^2 + c^2)^2}. \qquad (2)$$

Two aspect ratios, i.e., elongation index and flatness index, of the pore are calculated as b/a and c/b, respectively. Smaller values of elongation and flatness indices imply higher anisotropy in pore shape.

Fig. 6a–c presents the means (points) and standard deviations (error bars) of sphericity, elongation index and flatness index of pores at different strains. The pores in the initial sample are mostly spheroidal. Upon loading, the mean sphericity and aspect ratios all decrease with increasing strain. Therefore, the pore shapes deviate more and more from being spherical and show higher shape anisotropy during deformation and collapse. Pole figures of the a-axis orientation of the pores at different strains are presented in Fig. 6d. The pores are randomly oriented in the initial sample. The orientation distribution of pores changes significantly during deformation of the porous sample. However, no preferred orientation is observed for pores throughout the deformation process.
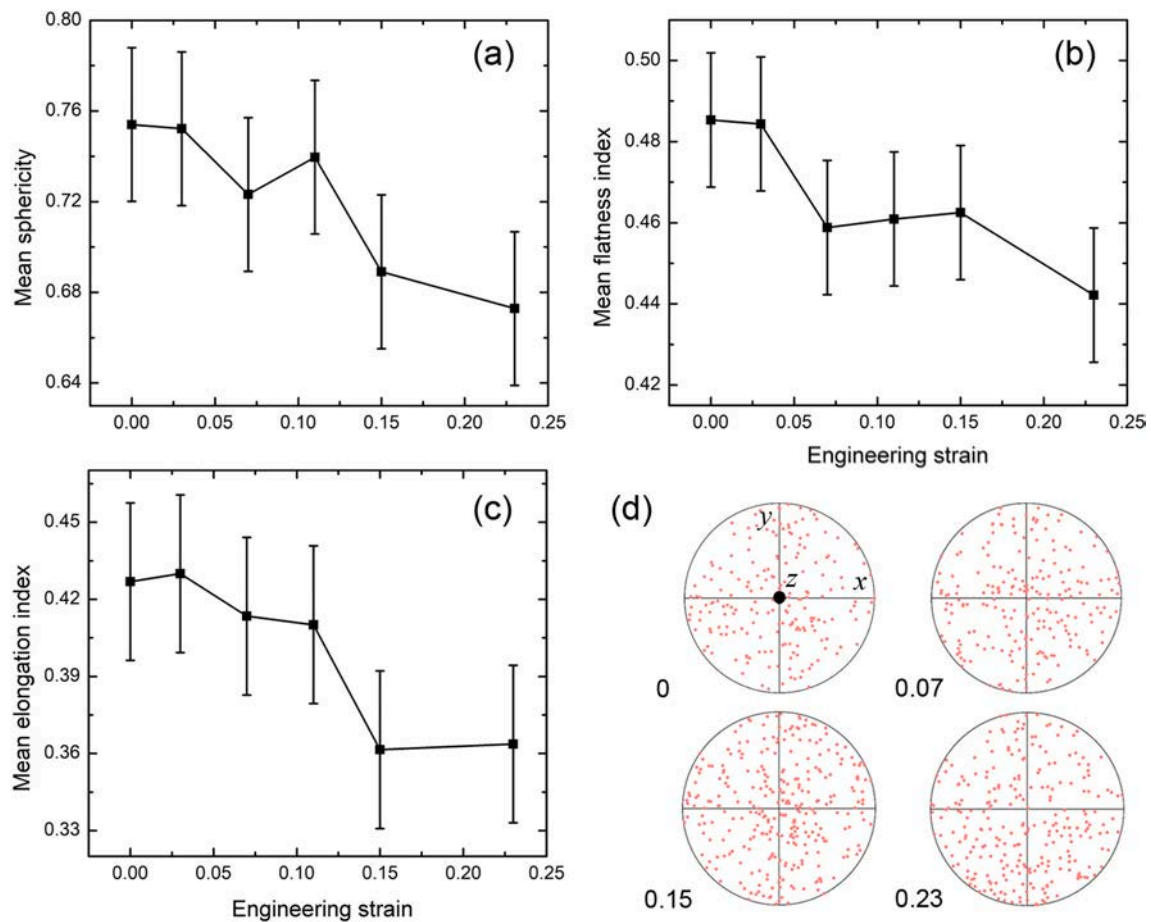
Fig. 6. Evolution of pore morphology with strain. (a) Sphericity. (b) Flatness index. (c) Elongation index. (d) Pole figures of the *a*-axis orientations of pores.
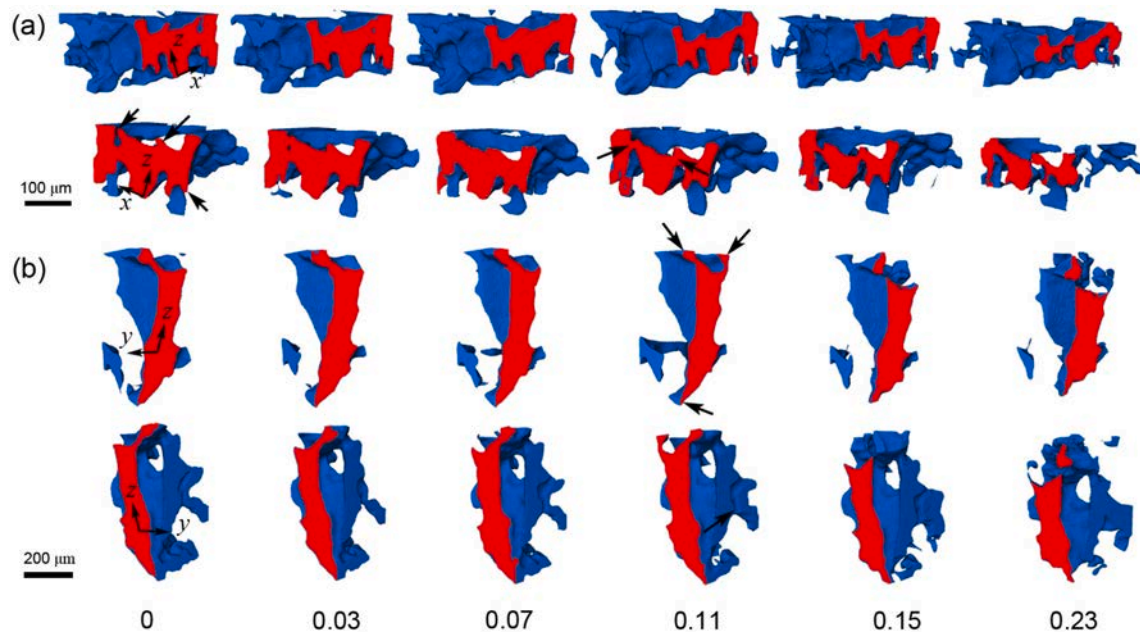

Fig. 7. 3D morphologies of two typical pores (H and V) at different bulk strains as marked, viewed from two different perspectives. (a) Pore H with its *a*-axis perpendicular to the loading direction. (b) Pore V with its *a*-axis parallel to the loading direction.

3.3. Pore deformation and collapse

To relate pore morphology with pore collapse, we track the

deformation and collapse of two typical pores, marked H (Fig. 7a) and V (Fig. 7b) for convenience. These two pores are both ellipsoidal, with a sphericity of 0.76 and 0.88, respectively. The elongation index and
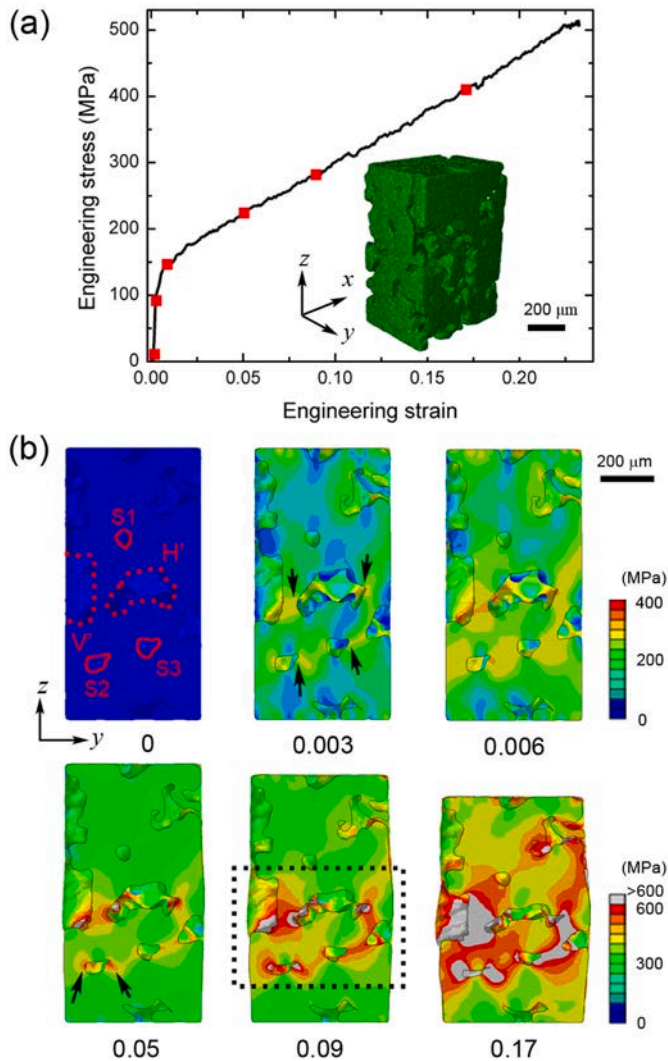
Fig. 8. FE modelling of the porous titanium. (a) Axial stress–strain curve. Inset: CT-derived 3D model of the initial porous sample. (b) Snapshots of the numerical sample (*yz* section) at different strains corresponding to the squares on the stress–strain curve. Color coding is based on the von Mises stress.

$$\sigma_{\max} = \sigma_0 \left(1 + \frac{l}{h}\right),\qquad(3)$$

where σ_0 is bulk stress, and l and h are pore axis lengths perpendicular and parallel to the loading direction, respectively. For pore H, $l > h$, while $l < h$ for pore V. Higher stress concentrations at the lateral walls lead to an earlier and fuller compaction of pore H. This explains qualitatively why pore V undergoes higher shrinkage than pore H, consistent with previous observations [18,7]. However, for porous Ti here, pores are not distributed in an infinite plate, and stress interactions occur between adjacent pores. The accurate stress distribution can be estimated via the mesoscale FE analysis.

3.4. FE modelling analysis

The axial stress–strain curve along with snapshots of the numerical sample at different axial strains (marked by squares) is shown in Fig. 8. The elastic modulus and yield strength of the numerical sample are 35 GPa and 138 MPa, respectively, much higher than the experimental measurements. The main reason is that the "digital" configuration for FE analysis (the inset of Fig. 8a) contains only smoothed macropores, and the exclusion of the sharp edges and corners of pores leads to an overestimation of stress [31,47]. However, it does not affect the qualitative discussions here; so we do not work on fitting the experimental curve using degraded material parameters of Ti, as done in previous studies [48]. A *yz*-section is chosen to show the structural evolution of inner pores. The *yz*-sections at different strains (marked in Fig. 8a) are presented in Fig. 8b. The von Mises stress σ_q^p is mapped onto the pore walls to monitor stress localizations.

Two pores similar to those in Fig. 7 exist in this *yz*-section, demarcated by the dashed curves at zero strain in Fig. 8b. The pore with its *a*-axis perpendicular or parallel to the loading direction (the *z*-axis) is marked H′ or V′. In the elastic deformation stage, stress concentrations occur in the lateral walls of pore H′ (marked by the arrows at $\varepsilon = 0.003$), and the maximum stress exceeds the yield stress (261.8 MPa). This explains why shrinkage occurs first in the lateral regions of pore H in Fig. 7a, and why throats are compacted at the elastic stage, as shown in Fig. 5d. Such stress concentrations intensify quickly with increasing loading and lead to the collapse of pore H′. In addition, stress concentration at the left wall of pore H′ propagates along the *y*-axis toward pore V′. Such stress interactions between adjacent pores lead to a heterogeneous stress distribution across the lateral walls of pore V′, and higher areas of plasticity across the sample as well. The position and value of the maximum stress for pore V′ is inconsistent with Eq. (3), because the Inglis' model is applicable to pores in an infinite plate. However, the average stress across the lateral wall of pore V′ is considerably smaller than that of pore H′. At $\varepsilon = 0.17$, pore V′ undergoes less shrinkage than pore H′, consistent with the experimental observations (Fig. 7).

For quasi-spherical pores (marked S1, S2 and S3 at zero strain in Fig. 8b), the stress states around them are dependent on their shapes. Stress concentrations occur on the sharp edges and corners of pores S2 and S3 (marked by the arrows at $\varepsilon = 0.003$). However, no obvious stress concentration occurs around pore S1 which has relatively smooth pore walls. In addition, when pore S2 is compacted and becomes ellipsoidal (similar to pore H′), stress concentrations occur in the two lateral walls of this flattened pore (marked by the arrows at $\varepsilon = 0.05$). Therefore, the increase in anisotropy of pore morphology leads to increasing stress concentration degree across the sample. In addition, a deformation band appears in the lower region of the sample, marked by the dashed rectangle at $\varepsilon = 0.09$. The location of this deformation band is consistent with that in the experiment, corresponding to the initial high-porosity region. Therefore, the numerical modelling reproduces the overall deformation characteristics observed in the experiments, including the compaction sequence of pores and the location of deformation banding.

flatness index are 0.49 and 0.22 for pore H, and are 0.57 and 0.47 for pore V. Pores H and V have similar elongation indices, but have *a*-axes aligned perpendicular and parallel to the loading axis, respectively. The pores are sliced into two parts along the loading direction and the cutting planes are marked in red, for better illustration of the pore collapse process.

Upon loading, the collapse process of two pores is different. For pore H, the edges and corners (marked by the arrows at zero strain, Fig. 7a) are firstly compacted at $\varepsilon = 0.03$. Above $\varepsilon = 0.07$, the lateral regions of pore H (marked by the arrows at $\varepsilon = 0.11$, Fig. 7a) shrink first and become slender throats at $\varepsilon = 0.15$. In contrast, pore V undergoes little deformation below $\varepsilon = 0.11$. Beyond that, the corners at the top and bottom ends (marked by the arrows at $\varepsilon = 0.11$, Fig. 7b) of the pore are compacted gradually. Pore V shrinks slightly along the loading direction and expands more along the lateral direction at $\varepsilon = 0.15$. However, pore V exhibits a much smaller volume reduction than pore H (24% versus 53%) at $\varepsilon = 0.23$, indicating that the pores oriented perpendicular to the loading direction are more prone to collapse.

For an infinite plate containing an elliptic pore, the maximum stress $\sigma_{\max}$ induced on the lateral walls of the pore can be estimated as follows [46],

4. Conclusions

In situ, synchrotron-based, micro CT is used to map the evolution of 3D microstructures of porous Ti under uniaxial compression, and the morphology of deformed pore structures is quantified with the PNM and gyration tensor analysis. The microstructure-based FE analysis reproduces the overall deformation characteristics observed in the experiments. The main conclusions are listed as follows.

- The overall porosity of the porous Ti sample decreases linearly with increasing bulk strain after sample yield. Compaction occurs firstly and concentrates in initially high-porosity region, leading to decreased structural heterogeneity across the sample.
- After sample yield, the mean values of equivalent diameter, sphericity and aspect ratios of pores decrease with increasing loading, indicating increased anisotropy of the pore morphology.
- The number and equivalent diameter of throats decrease starting from the elastic deformation stage, and the mean diameter of throats decreases linearly with increasing bulk strain throughout the deformation process.
- The spheroidal pores with their longest axis aligned perpendicular to the loading direction are more prone to collapse than those aligned parallel to the loading direction, because higher stress concentrations occur at the lateral regions of the former as revealed by the FE analysis.

Data availability

The raw data related to this manuscript would be made available on request.

Declaration of Competing Interest

The authors declare that they have no known competing financial interests or personal relationships that could have appeared to influence the work reported in this paper.

Acknowledgements

References

[1] S. Fujibayashi, M. Neo, H.-M. Kim, T. Kokubo, T. Nakamura, Osteoinduction of porous bioactive titanium metal, Biomaterials 25 (3) (2004) 443–450.

[2] J.R. Jones, G. Poologasundarampillai, R.C. Atwood, D. Bernard, P.D. Lee, Non-destructive quantitative 3D analysis for the optimisation of tissue scaffolds, Biomaterials 28 (7) (2007) 1404–1413.

[3] S.Y. Chen, C.N. Kuo, Y.L. Su, J.C. Huang, Y.C. Wu, Y.H. Lin, Y.C. Chung, C.H. Ng, Microstructure and fracture properties of open-cell porous Ti-6Al-4V with high porosity fabricated by electron beam melting, Mater. Charact. 138 (2018) 255–262.

[4] P. Heinl, L. Müller, C. Körner, R.F. Singer, F.A. Müller, Cellular Ti-6Al-4V structures with interconnected macro porosity for bone implants fabricated by selective electron beam melting, Acta Biomater. 4 (5) (2008) 1536–1544.

[5] K. Issen, T. Casey, D. Dixon, M. Richards, J. Ingraham, Characterization and modeling of localized compaction in aluminum foam, Scr. Mater. 52 (9) (2005) 911–915.

[6] S. Lee, F. Barthelat, N. Moldovan, H.D. Espinosa, H.N. Wadley, Deformation rate effects on failure modes of open-cell Al foams and textile cellular materials, Int. J. Solids Struct. 43 (1) (2006) 53–73.

[7] J.H. Zhao, Z.L. Xie, T. Zhong, T. Sun, K. Fezzaa, Y. Cai, J.Y. Huang, S.N. Luo, Strain rate effects on the mechanical behavior of porous titanium with different pore sizes, Mater. Sci. Eng. A (2021) 141593.

[8] L.J. Gibson, M.F. Ashby, Cellular Solids: Structure and Properties, Cambridge university press, 1999.

[9] N. Tuncer, G. Arslan, E. Maire, L. Salvo, Influence of cell aspect ratio on architecture and compressive strength of titanium foams, Mater. Sci. Eng. A 528 (24) (2011) 7368–7374.

[10] N. Tuncer, G. Arslan, E. Maire, L. Salvo, Investigation of spacer size effect on architecture and mechanical properties of porous titanium, Mater. Sci. Eng. A 530 (2011) 633–642.

[11] J.C. Li, D.C. Dunand, Mechanical properties of directionally freeze-cast titanium foams, Acta Mater. 59 (1) (2011) 146–158.

[12] S.J. Li, Q.S. Xu, Z. Wang, W.T. Hou, Y.L. Hao, R. Yang, L.E. Murr, Influence of cell shape on mechanical properties of Ti-6Al-4V meshes fabricated by electron beam melting method, Acta Biomater. 10 (10) (2014) 4537–4547.

[13] H.W. Chai, Z.L. Xie, X.H. Xiao, H.L. Xie, J.Y. Huang, S.N. Luo, Microstructural characterization and constitutive modelling of deformation of closed-cell foams based on in situ x-ray tomography, Int. J. Plasticity 131 (2020) 102730.

[14] S.K. Hyun, K. Murakami, H. Nakajima, Anisotropic mechanical properties of porous copper fabricated by unidirectional solidification, Mater. Sci. Eng. A 299 (1-2) (2001) 241–248.

[15] B.Q. Li, C.Y. Wang, X. Lu, Effect of pore structure on the compressive property of porous Ti produced by powder metallurgy technique, Mater. Design 50 (2013) 613–619.

[16] Z. Fan, B. Zhang, Y. Gao, X. Guan, P. Xu, Deformation mechanisms of spherical cell porous aluminum under quasi-static compression, Scr. Mater. 142 (2018) 32–35.

[17] H. Shen, L.C. Brinson, Finite element modeling of porous titanium, Int. J. Solids Struct. 44 (1) (2007) 320–335.

[18] R. Singh, P.D. Lee, T.C. Lindley, C. Kohlhauser, C. Hellmich, M. Bram, T. Imwinkelried, R.J. Dashwood, Characterization of the deformation behavior of intermediate porosity interconnected Ti foams using micro-computed tomography and direct finite element modeling, Acta Biomater. 6 (6) (2010) 2342–2351.

[19] M. Saadatfar, M. Mukherjee, M. Madadi, G.E. Schröder-Turk, F. Garcia-Moreno, F. M. Schaller, S. Hutzler, A.P. Sheppard, J. Banhart, U. Ramamurty, Structure and deformation correlation of closed-cell aluminium foam subject to uniaxial compression, Acta Mater. 60 (8) (2012) 3604–3615.

[20] B. Arifvianto, M.A. Leeflang, J. Zhou, Characterization of the porous structures of the green body and sintered biomedical titanium scaffolds with micro-computed tomography, Mater. Charact. 121 (2016) 48–60.

[21] Y.L. Sun, X. Zhang, Z. Shao, Q.M. Li, Image-based correlation between the meso-scale structure and deformation of closed-cell foam, Mater. Sci. Eng. A 688 (2017) 27–39.

[22] C. Lo, T. Sano, J.D. Hogan, Microstructural and mechanical characterization of variability in porous advanced ceramics using X-ray computed tomography and digital image correlation, Mater. Charact. 158 (2019) 109929.

[23] B.M. Patterson, N.L. Cordes, K. Henderson, J.J. Williams, T. Stannard, S.S. Singh, A.R. Ovejero, X. Xiao, M. Robinson, N. Chawla, In situ x-ray synchrotron tomographic imaging during the compression of hyper-elastic polymeric materials, J. Mater. Sci. 51 (1) (2016) 171–187.

[24] J.C. Cheng, H.W. Chai, G.L. Fan, Z.Q. Li, H.L. Xie, Z.Q. Tan, B.X. Bie, J.Y. Huang, S. N. Luo, Anisotropic spall behavior of CNT/2024Al composites under plate impact, Carbon 170 (2020) 589–599.

[25] R.C. Atwood, J.R. Jones, P.D. Lee, L.L. Hench, Analysis of pore interconnectivity in bioactive glass foams using X-ray microtomography, Scr. Mater. 51 (11) (2004) 1029–1033.

[26] J. Bock, A.M. Jacobi, Geometric classification of open-cell metal foams using X-ray micro-computed tomography, Mater. Charact. 75 (2013) 35–43.

[27] S. Jerban, S. Elkoun, Individual pore and interconnection size analysis of macroporous ceramic scaffolds using high-resolution X-ray tomography, Mater. Charact. 118 (2016) 454–467.

[28] K. Dixit, P. Gupta, S. Kamle, N. Sinha, Structural analysis of porous bioactive glass scaffolds using micro-computed tomographic images, J. Mater. Sci. 55 (27) (2020) 12705–12724.

[29] D.J. Lee, J.M. Jung, M.I. Latypov, B. Lee, J. Jeong, S.H. Oh, C.S. Lee, H.S. Kim, Three-dimensional real structure-based finite element analysis of mechanical behavior for porous titanium manufactured by a space holder method, Comp. Mater. Sci. 100 (2015) 2–7.

[30] Y.L. Sun, Q.M. Li, T. Lowe, S.A. McDonald, P.J. Withers, Investigation of strain-rate effect on the compressive behaviour of closed-cell aluminium foam by 3D image-based modelling, Mater. Design 89 (2016) 215–224.

[31] M. Doroszko, A. Seweryn, A new numerical modelling method for deformation behaviour of metallic porous materials using X-ray computed microtomography, Mater. Sci. Eng. A 689 (2017) 142–156.

[32] H. Shen, L.C. Brinson, A numerical investigation of porous titanium as orthopedic implant material, Mech. Mater. 43 (8) (2011) 420–430.

[33] N. Soro, L. Brassart, Y. Chen, M. Veidt, H. Attar, M.S. Dargusch, Finite element analysis of porous commercially pure titanium for biomedical implant application, Mater. Sci. Eng. A 725 (2018) 43–50.

[34] M.J. Blunt, M.D. Jackson, M. Piri, P.H. Valvatne, Detailed physics, predictive capabilities and macroscopic consequences for pore-network models of multiphase flow, Adv. Water Resour. 25 (8-12) (2002) 1069–1089.

[35] H.Y. Li, H.W. Chai, X.H. Xiao, J.Y. Huang, S.N. Luo, Fractal breakage of porous carbonate sand particles: microstructures and mechanisms, Powder Technol. 363 (2020) 112–121.

[36] G. Pyka, G. Kerckhofs, J. Schrooten, M. Wevers, The effect of spatial micro-CT image resolution and surface complexity on the morphological 3D analysis of open porous structures, Mater. Charact. 87 (2014) 104–115.

[37] D. Gürsoy, F. De Carlo, X. Xiao, C. Jacobsen, TomoPy: a framework for the analysis of synchrotron tomographic data, J. Synchrotron Radiat. 21 (5) (2014) 1188–1193.

[38] A.A. Melkman, On-line construction of the convex hull of a simple polyline, Inform. Process. Lett. 25 (1) (1987) 11–12.

[39] Z. Li, D. Liu, Y. Cai, P. Ranjith, Y. Yao, Multi-scale quantitative characterization of 3-D pore-fracture networks in bituminous and anthracite coals using FIB-SEM tomography and X-ray μ-CT, Fuel 209 (2017) 43–53.

[40] J. Lin, J. Li, T. Liu, Z. Xie, L. Zhu, Y. Wang, Y. Guan, Investigation on ultrasonic vibration effects on plastic flow behavior of pure titanium: Constitutive modeling, J. Mater. Res. Technol. 9 (3) (2020) 4978–4993.

[41] N. Wang, E. Maire, Y. Cheng, Y. Amani, Y. Li, J. Adrien, X. Chen, Comparison of aluminium foams prepared by different methods using X-ray tomography, Mater. Charact. 138 (2018) 296–307.

[42] M.A. Kader, A.D. Brown, P.J. Hazell, V. Robins, J.P. Escobedo, M. Saadatfar, Geometrical and topological evolution of a closed-cell aluminium foam subject to drop-weight impact: an X-ray tomography study, Int. J. Impact Eng. 139 (2020) 103510.

[43] R. Singh, P.D. Lee, T.C. Lindley, R.J. Dashwood, E. Ferrie, T. Imwinkelried, Characterization of the structure and permeability of titanium foams for spinal fusion devices, Acta Biomater. 5 (1) (2009) 477–487.

[44] A. Handan, J. Wolfhard, Gyration tensor based analysis of the shapes of polymer chains in an attractive spherical cage, J. Chem. Phys. 138 (5) (2013), 520–140.

[45] Y. Yao, H.W. Chai, C. Li, B.X. Bie, X.H. Xiao, J.Y. Huang, M.L. Qi, S.N. Luo, Deformation and damage of sintered low-porosity aluminum under planar impact: microstructures and mechanisms, J. Mater. Sci. 53 (6) (2018) 4582–4597.

[46] C.E. Inglis, Stresses in a plate due to the presence of cracks and sharp corners, Trans. Inst. Naval Archit. 55 (1913) 219–241.

[47] M. Doroszko, A. Seweryn, Pore-scale numerical modelling of large deformation behaviour of sintered porous metals under compression using computed microtomography, Mech. Mater. 141 (2020) 103259.

[48] M. Doroszko, A. Seweryn, Numerical modeling of the tensile deformation process of sintered 316L based on microtomography of porous mesostructures, Mater. Design 88 (2015) 493–504.